ISSN 1392-1320 MATERIALS SCIENCE (MEDŽIAGOTYRA). Vol. XX, No. X. 2027

Wear and Corrosion Resistance of HVOF-Sprayed CoCrNi Medium Entropy Alloy Coatings

Yueming WANG [1], Ting XIA [1], Lu XIE [2] *

[1] *School of Materials Science and Engineering, Hunan University of Science and Technology, Xiangtan 411201, China*
[2] *School of Management Engineering, Jiangsu Urban and Rural Construction Vocational College, Changzhou 213147, China*

http://doi.org/10.5755/j02.ms.44008

Received 4 January 2026; accepted 27 February 2026

CoCrNi medium entropy alloy (MEA) coatings were prepared by high velocity oxy-fuel (HVOF) spraying. The microstructures, wear resistance in a wide temperature range, corrosion resistance in NaCl and NaOH solutions of the MEA coatings were systematically studied by SEM, XRD, friction experiment, and electrochemical corrosion test. The microstructure of HVOF coatings was uniform with FCC single-phase solid solution. As the friction temperature increased from room temperature to 200 °C, 400 °C, and 600 °C, the friction coefficients, wear track depth and width, and wear volume loss of the coatings gradually decreased. And these parameters of CoCrNi coating at 600 °C are about 0.50 ± 0.1, (140 ± 8) μm, (2.10 ± 0.1) mm, (0.0234 ± 0.0001) g, respectively. Abrasive wear, fatigue wear and plastic deformation were the main wear mechanisms of CoCrNi coatings during the wear test at room temperature. And oxidation wear became the main wear mechanism of CoCrNi coating during the wear test at 400 °C and 600 °C. E_{corr} and I_{corr} of the CoCrNi coatings in NaCl solution were approximately (-0.217 ± 0.01) mV and (0.26 ± 0.08) $\mu A/cm^2$, respectively. E_{corr} and I_{corr} of CoCrNi coatings in NaOH solution were approximately (-0.282 ± 0.02) and (0.04 ± 0.01) $\mu A/cm^2$, respectively. And the corrosion resistance of CoCrNi coatings were more superior than 45 carbon steel.

Keywords: high velocity oxy-fuel spraying, CoCrNi medium entropy alloy, wear resistance.

1. INTRODUCTION*

Traditional alloy designers believed that many unfavorable phases appeared in an alloy as it changed from single component to multiple ones. Then the performance of the alloy would be weakened. Yeh broke the shackles of conventional alloys in the 1990s and he proposed a new design idea of high entropy alloys (HEAs) for the first time [1, 2]. HEAs, a new alloy system consisting of 5 – 35 % of each component, were developed by Yeh et al. [3]. Since then, HEAs have attracted wide attention due to their high wear and corrosion resistance, excellent machinability, and outstanding thermal resistance [4 – 8]. Recently, investigations of HEAs have been extended to medium entropy alloys (MEAs) [9 – 10], which are equal-atomic alloys composed of two to four main elements. Due to superior mechanical properties [11] and excellent corrosion resistance [12], CoCrNi, as a representative MEAs has been widely used in extreme environments. After a series of multi-component isoatomic solid solution alloys with FCC structure being investigated, Wu et al. [13] found that CoCrNi ternary alloy with a Vickers hardness of 550 HV (equivalent to about 5.4 GPa) was the hardest of all. Gludovatz et al. [14] pointed out that isoatomic MEAs, as one of FCC solid solutions, showed superior strength-toughness properties than most multiphase alloys. Rodriguez et al. [15] found that the corrosion resistance of CoCrFeMnNi HEA group in CO_2-containing acidic sodium chloride solution was enhanced by the presence of Cr. The corrosion behaviors of CoCrFeMnNi HEA coating and SS304L in 0.1 M H_2SO_4 solution were compared by Luo et al. [16]. And they revealed that the poor corrosion resistance of CoCrFeMnNi coating was related to the low Cr content and formation of a large amount of metal hydroxides in the passivation film. Both CoCrNi MEAs and CoCrFeMnNi HEAs have the same lattice structure and similar mechanical properties. Then it is worth to investigate the corrosion behavior of isoatomic CoCrNi MEAs. CoCrNi MEA coatings have been prepared by magnetron sputtering [17 – 19], laser cladding [20 – 21] and plasma cladding [22]. Since metal powders can be heated up and accelerated in high temperature and high speed flame flow, thermal spraying has been proven to be an effective method to prepare protective coatings with superior wear resistance, corrosion resistance, heat resistance, and oxidation resistance on metal surfaces. As a type of thermal spray technology, HVOF has lower combustion oxygen content and therefore lower temperature, which is essential to reduce decomposition or excessive oxidation during spraying. Then HVOF is suitable for preparation coatings which are easily oxidized, such as CoCrNi MEAs coatings.

However, only a few researches [23 – 25] of CoCrNi MEA coatings prepared by HVOF have been reported until today. Furthermore, tribological behaviors (in a wide temperature range) and electrochemical corrosion properties (in various corrosive solutions) of CoCrNi MEA coatings have not been systematically investigated yet. As a result, CoCrNi MEA coatings were prepared on 45 carbon steel by HVOF here. The tribological properties

---

* Corresponding author: L. Xie
E-mail: *010640@jscc.edu.cn*

of CoCrNi MEA coatings were investigated in a wide temperature range. The electrochemical corrosion resistances of CoCrNi coatings were evaluated in NaCl and NaOH solutions, respectively.

2. EXPERIMENTAL PROCESS

2.1. HVOF spraying

Before spraying, the matrix surfaces were cleaned by acetone, and then sandblasted with 120 # (0.125 mm) brown corundum sand under 0.2 MPa pressure. Spherical particles with uniform microstructure and component can be found in CoCrNi MEA feedstock (see Fig. 1), which were prepared by gas atomization.

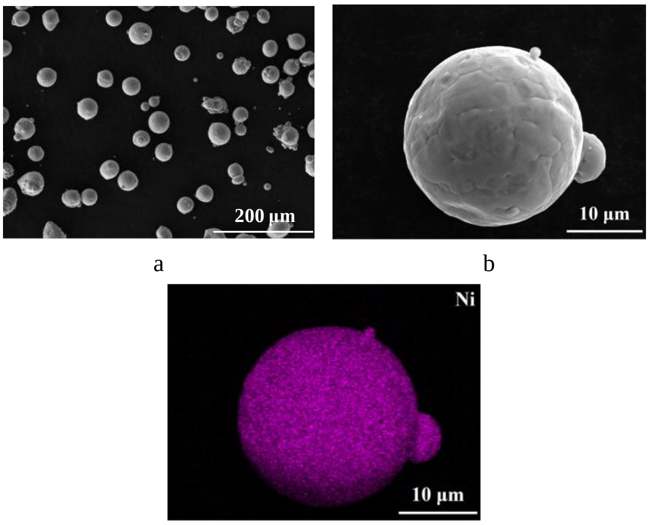

a b

c

Fig. 1. SEM images and EDS map distribution of CoCrNi MEA feedstock: a – panorama; b – high magnification image; c – Ni element distribution of a single powder

The particle size of CoCrNi MEA powders was distributed from 10 µm to 80 µm. And the average particle size was 40 µm. CoCrNi MEA coatings were prepared on 45 carbon steel by a HVOF spraying system (Praxair, JP8000, USA), which used aviation kerosene, oxygen, and nitrogen as fuel, combustion improver, and carrier gas, respectively. And spraying parameters including kerosene flow rate, oxygen flow rate, carrier gas flow rate and powder feeding rate were 10 $L \cdot h^{-1}$, 35 $m^3 \cdot h^{-1}$, 300 $L \cdot h^{-1}$, and 10 $r \cdot min^{-1}$, respectively.

2.2. Friction and wear test

The tribological experiments of CoCrNi MEA coating at a wide temperature range were carried out on a GF-I high temperature friction and wear tester. The friction load, rotation speed and wear time was 60 N, 600 $r \cdot min^{-1}$, and 30 min, respectively. The reciprocating length of Si_3N_4 grinding balls with diameter of 6 mm was 5 mm here. The friction temperatures of this work were room temperature, 200, 400, and 600 ℃, respectively. The friction coefficient is recorded by a computer. The MT-500 probe-type material surface wear mark measuring instrument was used to analyze the cross-sectional morphology of wear scars and calculate the wear volume loss. The running length of the probe was 5 mm [26].

2.3. Electrochemical corrosion test

The electrochemical corrosion behaviors of the CoCrNi MEA coatings and 45 carbon steel at room temperature were investigated by the polarization method in 3.5 mass % NaCl solution and 0.1 M NaOH solution using an electrochemical workstation (CHI660E, Shanghai Chenhua Instrument Co., Ltd., China). The specimens were polished to a mirror surface, and sealed which epoxy resin to expose an area of 1 cm × 1 cm for the corrosion test. During the corrosion test, a conventional three-electrode cell was used, with a coating sample, saturated calomel electrode (SCE), and platinum foil as working, reference, and auxiliary electrode, respectively. The potential was scanned at a sweep rate of 1 mV/s from -700 to 1500 mV relative to open-circuit potential (OCP). The electrochemical test was repeated three times to ensure the accuracy of the data.

2.4. Microstructure and phase composition analysis

The morphology of initial feedstock, HVOF coating, wear debris, worn surfaces of HVOF coating and Si_3N_4 grinding ball, electrochemical corrosion surfaces of HVOF coating, and 45 carbon steel were tested by using a scanning electron microscope (Tescan Mira4, Tescan Orsay Holding, Czech Republic). The element distribution was analyzed by an energy-dispersive spectrometer (AztecLiveOneX plore 30, Oxford, UK). The phase composition of MEA powder and HVOF coating was analyzed by x-ray diffractometer (Bruker D8 Advance, Bruker, Germany) with CuKα wavelength of 1.54056 A°, and the voltage, current, scanning rate and step size were 40 kV, 40 mA, 2 °/min, and 0.02°, respectively. The scanning range was from 0° to 100°. The particle size of CoCrNi powder was measured by the LA-950 laser particle size analyzer.

3. RESULTS AND DISCUSSION

3.1. Morphology and phase analysis of HVOF coating

Cross-section images of HVOF CoCrNi coatings are shown in Fig. 2. The thickness of the CoCrNi coating is about (994 ± 10) µm as shown in Fig. 2 a. Deposition of CoCrNi powders mainly relied on high kinetic energy collision during HVOF spraying. And then CoCrNi coatings displayed a granular structure (see Fig. 2 b and c) for initial powders that were not completely melted and spread into layered structures during HVOF spraying. In addition, there are a few micropores that can be found in the HVOF coating as shown in Fig. 2 b and c. Dark particles, which were caused by the insertion of Al_2O_3 powders into the surface of matrix during sandblasting, can be observed in the bonding interface (see Fig. 2 c).

The EDS results of the cross-section of CoCrNi coating are shown in Fig. 3. It can be observed that the Co element is evenly distributed in the HVOF coating (see Fig. 3 b). EDS maps of Cr and Ni elements are not provided here for simplification. O element can be found at the interface of innerlayers of CoCrNi coating as shown in local magnification areas (see Fig. 3 d and f).

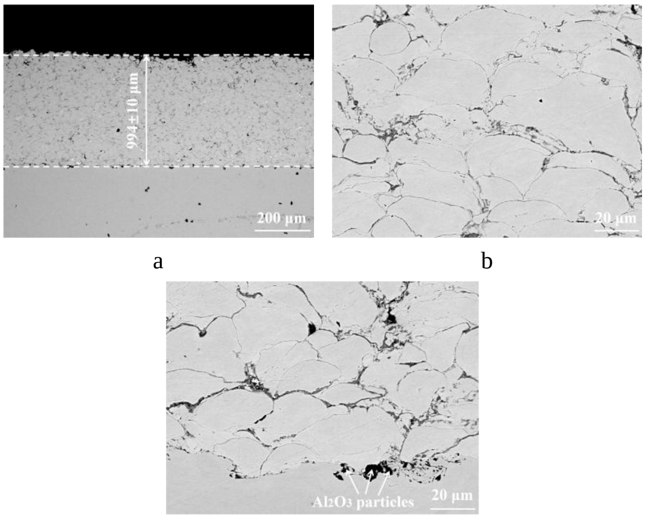

a b

c

Fig. 2. SEM images of CoCrNi MEA coatings: a – panorama; b – local magnification image of inner coatings; c – local magnification image of interface region

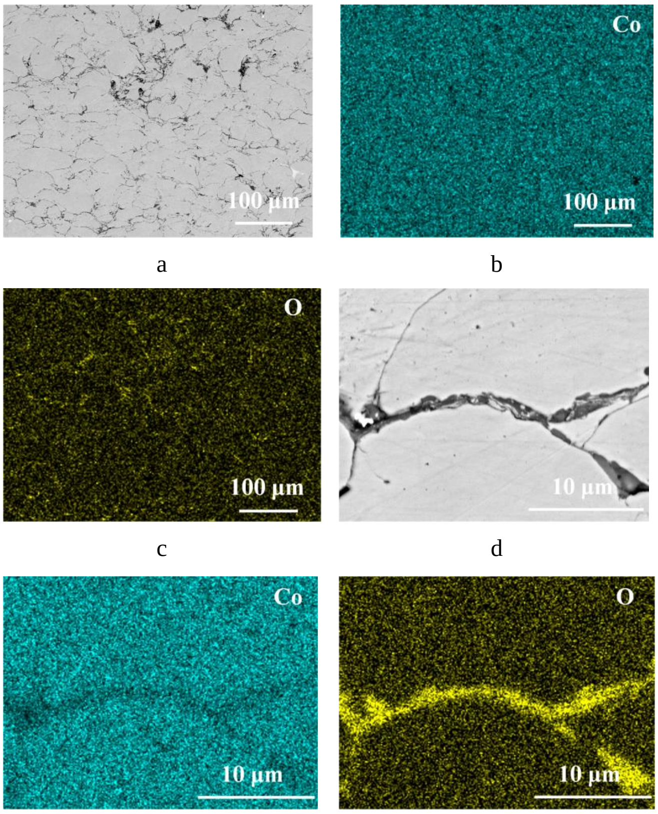

a b

c d

e f

Fig. 3. SEM image of EDS maps selected area and element map distributions of HVOF coatings: a – low magnification image of selected area; b – Co element map distribution; c – O element map distribution; d – high magnification image of interface area of innerlayers; e – Co element map distribution; f – O element map distribution

Results of EDS maps of CoCrNi powder and HVOF coating are shown in Table 1. CoCrNi MEA feedstock prepared by gas atomization was a kind of oxygen free material. Due to slight oxidation of powder surfaces during spraying, oxygen contents in the panorama and innerlayer interface area of HVOF coatings increased up to 3.95 at.% and 5.61 at.%, respectively.

Table 1. EDS map results of CoCrNi powder and HVOF coating

Sample	Co	Cr	Ni	O
	at.%			
MEA powder	32.50	32.20	35.30	0.00
panorama of HVOF coating	31.23	30.77	34.05	3.95
interface of innerlayers of HVOF coating	30.82	33.41	30.16	5.61

The XRD patterns of CoCrNi powder and HVOF coatings are shown in Fig. 4.

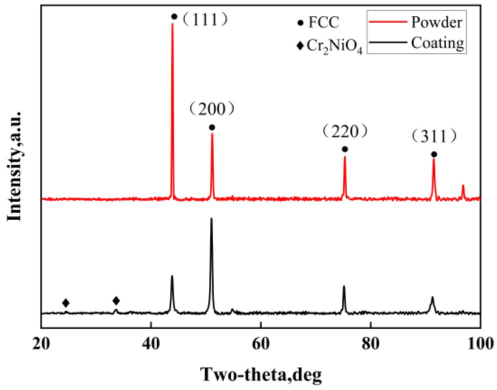

Fig. 4. XRD patterns of CoCrNi powder and HVOF coatings

Both powder and coating have crystalline peaks corresponding to the crystal planes (111), (200), (220) and (311) of FCC single-phase solid solution. Compared to the XRD patterns of the feedstock, those of the HVOF coatings basically have no large angle deviation, and the FCC structures still maintained, indicating that the coatings are dense and uniform. However, weak oxide peaks appeared at 23.12°and 36.26° of XRD patterns of HVOF coating. It can be concluded mild oxidation occurred and Cr_2NiO_4 phase formed during spraying. Similar results have been reported in the work of Koga et al. [23].

3.2. Friction and wear test

The COF-time curves and wear track marks of HVOF CoCrNi coatings in a wide temperature range are shown in Fig. 5. The friction coefficients in the steady stage at room temperature, 200, 400, and 600 °C were (1.40 ± 0.03), (1.00 ± 0.02), (0.75 ± 0.04), and (0.50 ± 0.01), respectively. The average friction coefficient gradually decreased with increasing of friction temperature. All of the four friction coefficients rose rapidly at first and then tended to be stable during running-in. The wear track depth of CoCrNi coatings (see Fig. 5 b) at room temperature, 200, 400, and 600 °C were (450 ± 10), (397 ± 12), (190 ± 9) and (140 ± 8) μm, respectively. The average wear rates of CoCrNi coatings at room temperature, 200, 400, and 600 °C are $(43.88 \pm 0.50) \times 10^{-5}$, $(40.81 \pm 0.40) \times 10^{-5}$, $(14.72 \pm 0.20) \times 10^{-5}$, and $(7.99 \pm 0.10) \times 10^{-5}$ $mm^3/(N{\cdot}m)$, respectively. It can be concluded that HVOF CoCrNi coatings have excellent high temperature wear resistances.

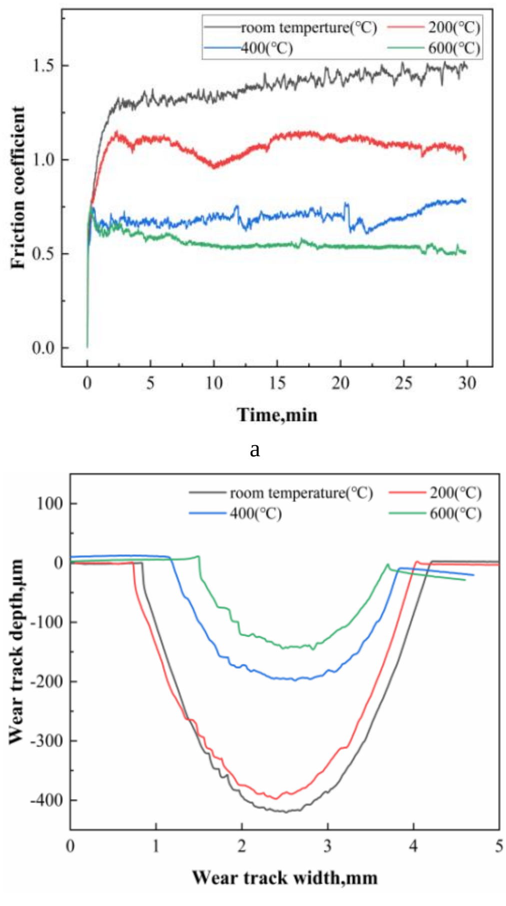

a

b

Fig. 5. a – COF-time curves; b – wear track marks of HVOF CoCrNi coatings

Morphologies of worn surfaces of CoCrNi coatings are shown in Fig. 6. The width of wear scars of CoCrNi coating after wear test for 30 min under room temperature is about 4.11 mm, as shown in Fig. 6 a. Spalling holes, wear debris, and microcracks perpendicular to the moving direction of grinding balls can be observed in local magnification images (see Fig. 6 b and c). The wear mark width of the coating decreases to 3.46 mm as friction temperature increases to 200 °C (see Fig. 6 d). Friction grooves parallel to the moving direction of grinding balls are formed in the local magnification image, as shown in Fig. 6 e and f. In addition, spalling and wear debris can be found in Fig. 6 e and f, respectively. As the friction temperature further increased up to 400 °C and 600 °C, the wear mark widths of CoCrNi coating reduced to 2.59 mm (see Fig. 6 g) and 2.20 mm (see Fig. 6 j), respectively. Wear debris, spalling holes, microcracks and adhesive layers can be found in wear scars of CoCrNi coatings as shown in Fig. 6 h, i, k, and l. Abrasive wear, fatigue wear and plastic deformation were the main wear mechanisms during room temperature friction, while abrasive wear, adhesive wear, fatigue wear, and other wear mechanisms (for example, oxidative wear) occurred during high temperature test.

After wear test at room temperature for 30 min, light grey phase and dark grey one can be observed in the worn surface of CoCrNi coating as shown in Fig.7 a.

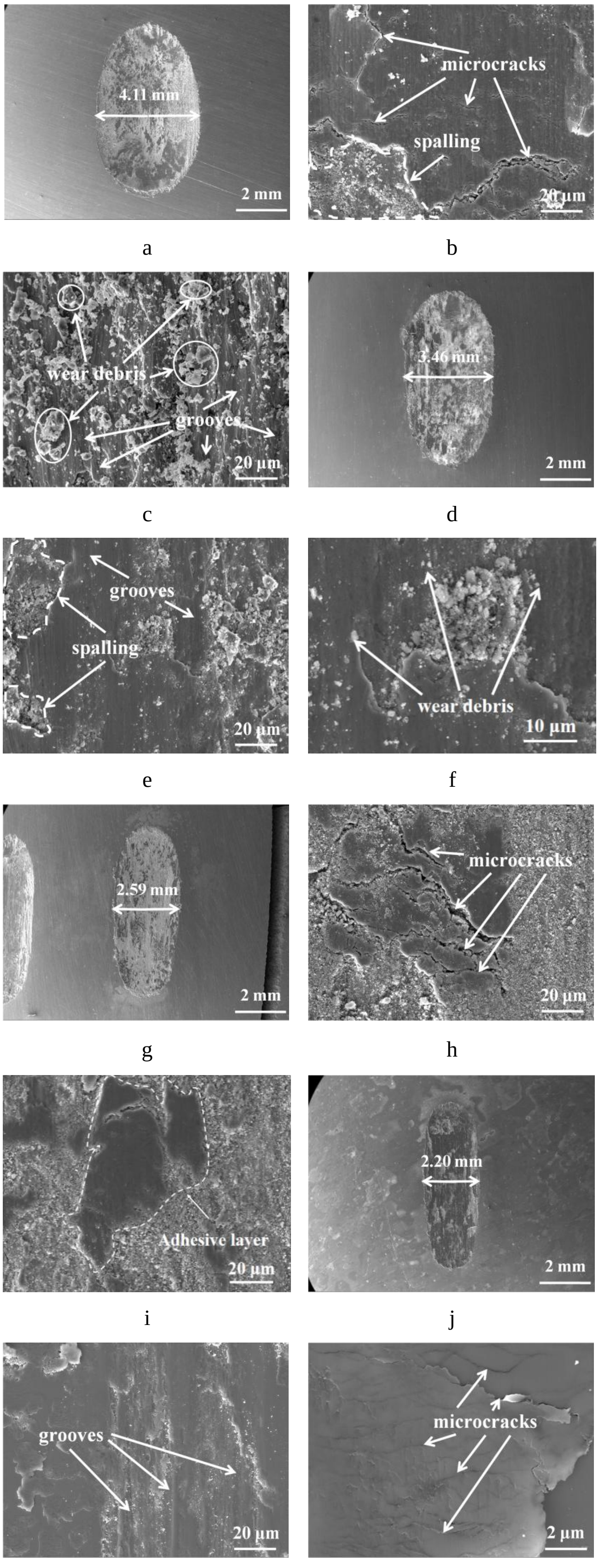

a

b

c

d

e

f

g

h

i

j

k

l

Fig. 6. Panorama and local magnification morphologies of worn surfaces of HVOF coatings after wear test at different temperatures: a, b, c – room temperature; d, e, f – 200 °C; g, h, i – 400 °C; j, k, l – 600 °C

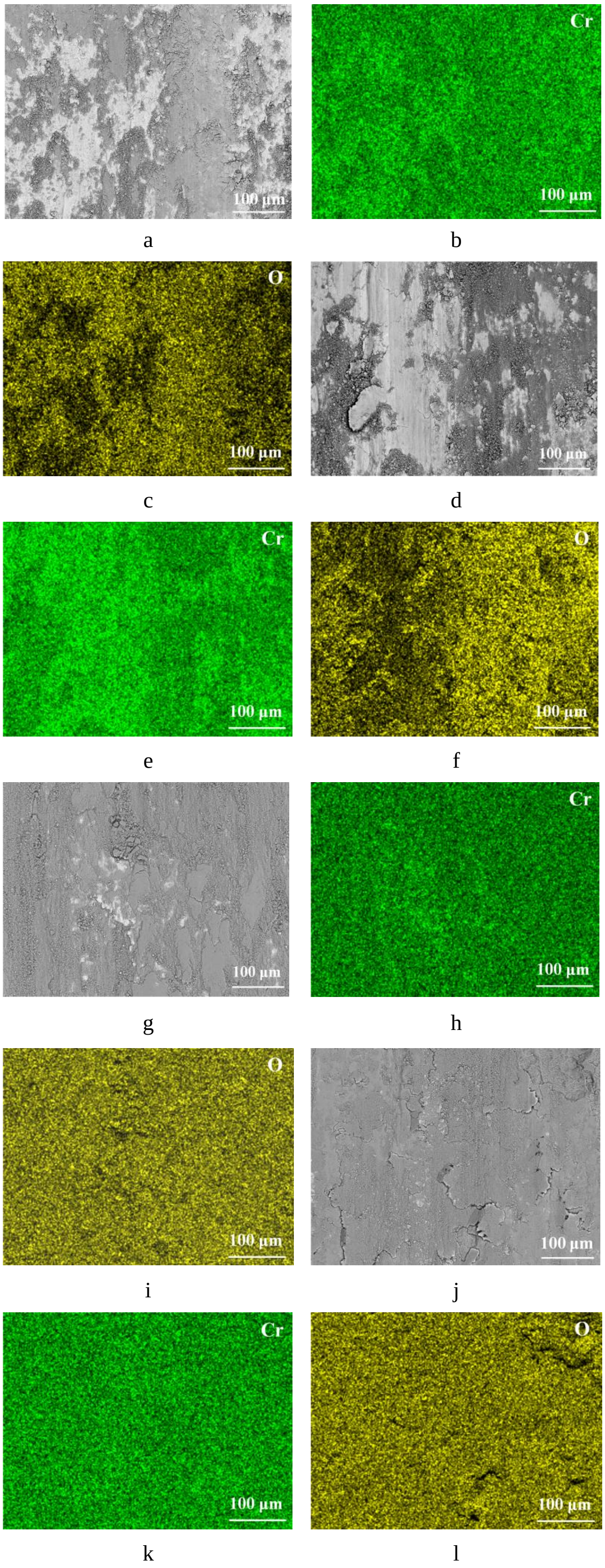

Fig. 7. EDS detected area, Cr and O element map distributions of worn surfaces of HVOF coatings after wear test at different temperatures: a, b, c – room temperature; d, e, f – 200 °C; g, h, i – 400 °C; j, k, l – 600 °C

Cr and O element concentrated in light grey phase area and dark grey one (see Fig. 7 b and c), respectively. Co and Ni element map distributions were not provided in this work for simplification. Similar phenomena can be found in the worn surfaces of CoCrNi coating (see Fig. 7 d and f after wear test at 200 °C for 30 min. As the friction temperature rose to 400 and 600 °C, the amount of dark grey phase in the worn surfaces of CoCrNi coating increased markedly as shown in Fig. 7 g and j, respectively. Oxygen contents of worn surfaces of CoCrNi coatings after room temperature and 200 °C wear tests were 11.35 mass % and 10.56 mass %, respectively. As the temperature rose to 400 and 600 °C, the oxygen contents of worn surfaces of HVOF coatings were increased up to 23.16 mass % and 24.11 mass %, respectively. As a result, oxidation wear became one of the main wear mechanisms of HVOF coatings during 400 and 600 °C friction tests. In addition, oxidation wear has been found in HVOF sprayed TiB_2-50Ni coating (Ref. 26), HVAF sprayed eutectic HEA coatings [27], detonation sprayed iron-based amorphous alloy coatings [28, 29] and APS FeCoCrNi HEA coatings [30] during high temperature wear tests.

The diameters of wear scars of Si_3N_4 dual grinding balls are significantly affected by friction temperatures (see Fig. 8). The diameter of wear scars of Si_3N_4 balls after wear test at room temperature for 30 min was about 3462.7 μm, as shown in Fig. 8 a. They decreased to about 3135.5 μm (see Fig. 8 d), 2448.5 μm (see Fig. 8 g) and 2213.9 μm (see Fig. 8 j) as the friction temperature increased up to 200, 400 and 600 °C, respectively. It should be noted that the change trend of wear scars of Si_3N_4 grinding balls is consistent with the wear track width of HVOF coating as shown in Fig. 6. In addition, the white phase in wear scars were proved to be oxides by Cr and O element map distributions as shown in Fig. 8 b, c, e, f, h, i, k, and l. Similarly, Co and Ni elements map distributions were not provided here for simplicity. Note here, smooth oxide films formed on the surface of the wear scars of Si_3N_4 balls as shown in Fig. 8 h, i and k, l. As a result, the friction coefficient, wear track depth and width, wear rate of CoCrNi coating ($\geq$ 400 °C) decreased obviously owing to the formation of stable oxide films both on the worn surfaces of HVOF coating and wear scars of Si_3N_4 balls. The protective and solid lubricating effects of oxide films were further confirmed here. Then the abrasive wear and adhesive wear of the MEA coating were weakened during high temperature friction.

SEM morphologies of wear debris collected from CoCrNi coatings after wear test at different temperatures for 30 min were shown in Fig. 9. Fine particles and plate-like ones can be observed in wear debris collected from room temperature, 200 °C and 400 °C friction experiment as shown in Fig. 9 a, b, and c. Most of wear debris collected from 600 °C friction experiment are plate-like particles as shown in Fig. 9 d. Oxidative wear accelerated as the temperature increased up to 600 °C.

More oxides formed and then deformed into a thin film on the worn surface during the continuous wear test. Finally, the oxide film cracked and peeled off. As the result, most of the plate-like wear debris can be collected after 600 °C wear test.

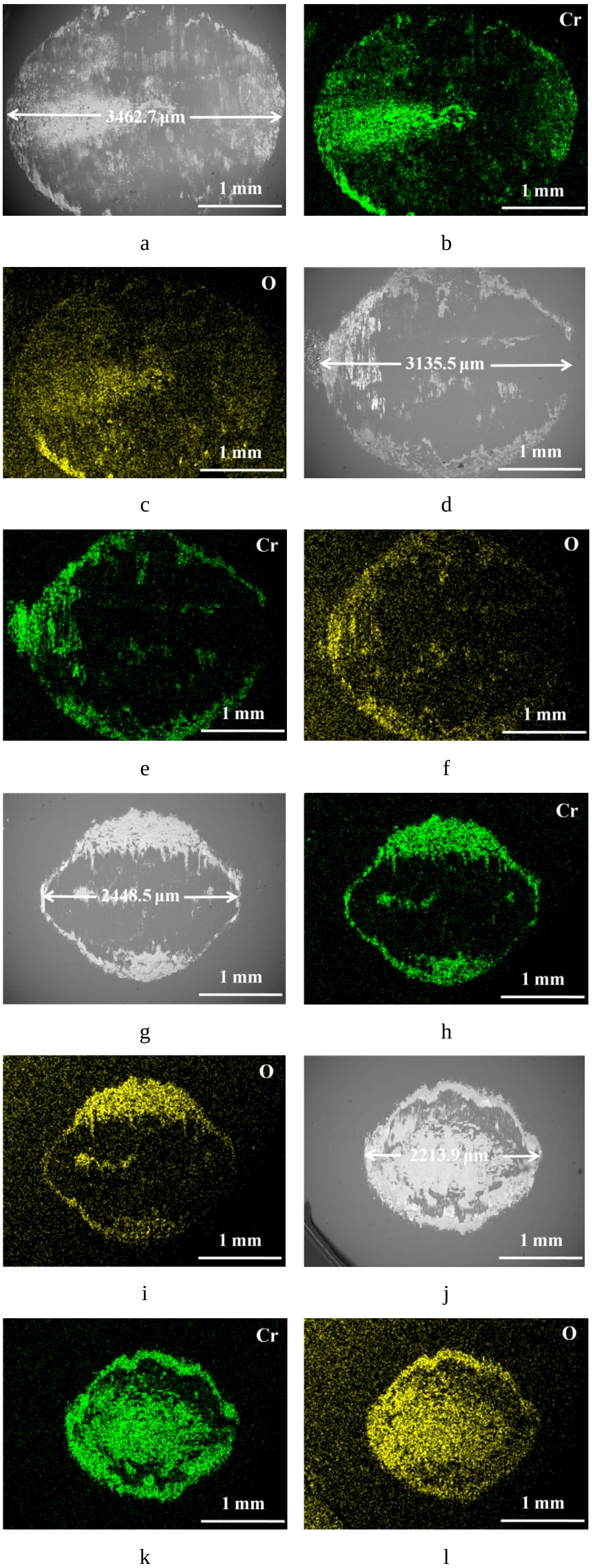

a b c d e f g h i j k l

Fig. 8. SEM images (SE), Cr and O element map distributions of wear scars of Si_3N_4 balls after wear test at different temperatures: a, b, c – room temperature; d, e, f – 200 °C; g, h, i – 400 °C; j, k, l – 600 °C

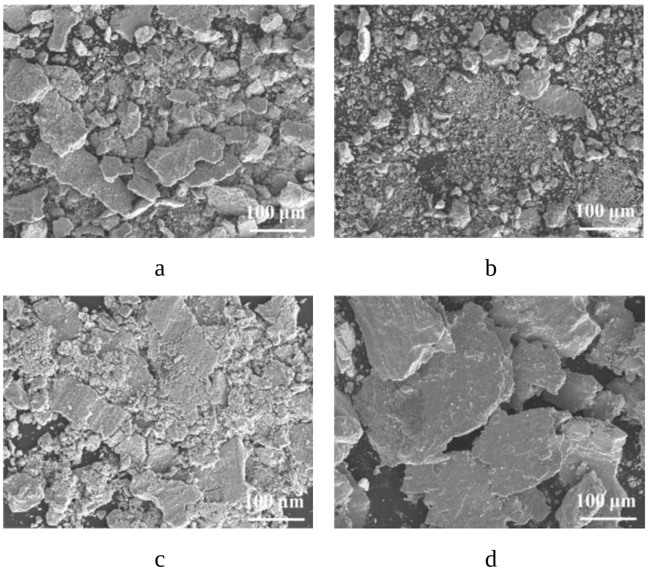

a b c d

Fig. 9. SEM images of wear debris of HVOF coatings after wear test at different temperatures: a – room temperature; b – 200 °C; c – 400 °C; d – 600 °C

3.3. Potentiodynamic polarization test

Potentiodynamic polarization curves of the CoCrNi coating and 45 carbon steel in 3.5 wt.% NaCl solutions and 0.1M NaOH solutions at room temperature are shown in Fig. 10.

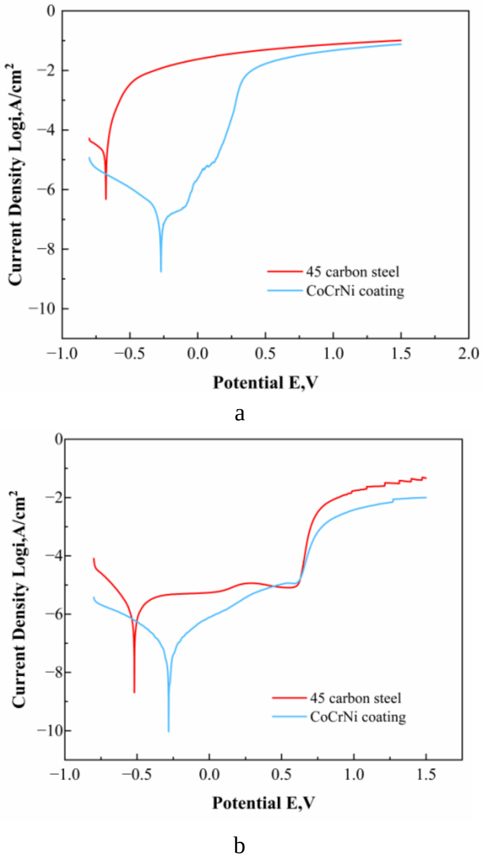

a

b

Fig. 10. Potentiodynamic polarization curves of the CoCrNi coatings and 45 carbon steel in: a – 3.5 wt.% NaCl solution; b – 0.1M NaOH solution at room temperature

The potentiodynamic polarization curves of the anode and cathode regions were performed by Tafel extrapolation method to obtain the values of corrosion potential (E_{corr}) and corrosion current density (I_{corr}). Main corrosion electrochemical parameters, such as corrosion potential (E_{corr}), cathodic (βc), anodic (βa) slops and the linear polarization resistance (R), are listed in Table 2. E_{corr} and I_{corr} of the CoCrNi coatings in NaCl solution are approximately (-0.217 ± 0.01) mV and (0.26 ± 0.08) µA/cm^2, respectively. And those of 45 carbon steel are (-0.677 ± 0.02) mV and (50.9 ± 0.04) µA/cm^2, respectively. E_{corr} of the CoCrNi coating was higher than that of 45 carbon steel, while I_{corr} of the former was lower than that of the latter. Similarly, compared to 45 carbon steel, the CoCrNi MEA coating in NaOH solution exhibited a higher corrosion potential of (-0.282 ± 0.02) mV and a lower corrosion current density of (0.04 ± 0.01) µA/cm^2. It can be concluded that the corrosion resistances of CoCrNi coating both in NaCl and NaOH solutions were superior than those of 45 carbon steel owing to the higher E_{corr} and lower I_{corr} values. The parameter R correlates to the electric resistance of the material to corrosion. The larger the value of R is, the higher the barrier of materials to corrosion is [31, 32]. The R values of the CoCrNi coating were higher than those of 45 carbon steel in 3.5 wt.% NaCl and 0.1 M NaOH solutions here. These all confirmed the excellent corrosion resistance of CoCrNi coatings.

3.4. Morphology of corroded surfaces

Fig. 11 shows the surface morphologies of the CoCrNi coatings and 45 carbon steel after immersion in 3.5 wt.% NaCl solutions at room temperature. The defects on the surface of CoCrNi coating are considered as corrosion pits as shown in Fig. 11 a. The main chemical components of black, dark grey and light grey zones of CoCrNi coating are listed in Table 3.

The black and dark grey zone are metastable pits distributed randomly on the surface of HVOF coatings. The dark grey area was proven to be oxide film which perhaps formed during HVOF spraying or electrochemical corrosion. The light grey area of CoCrNi coating had hardly been corroded during electrochemical corrosion. The black corrosion pits were rich of Cr and O elements. And the Chromium oxides played a protective role in the black zone (see Fig. 11 a).

Comparing to CoCrNi coatings, a large amount of rough corrosion products can be found on the surface of 45 carbon steel as shown in Fig. 11 b. The corrosion zones were rich of Fe and O elements. The electrochemical reaction of 45 carbon steel in NaCl solutions was the cathodic depolarization control process. The combination of cathodic Cl$^-$ and Fe^{2+} generates H$^+$ and Cl$^-$, which promote the ionization of anodic Fe and accelerate the corrosion of Fe elements in 45 carbon steel [33].

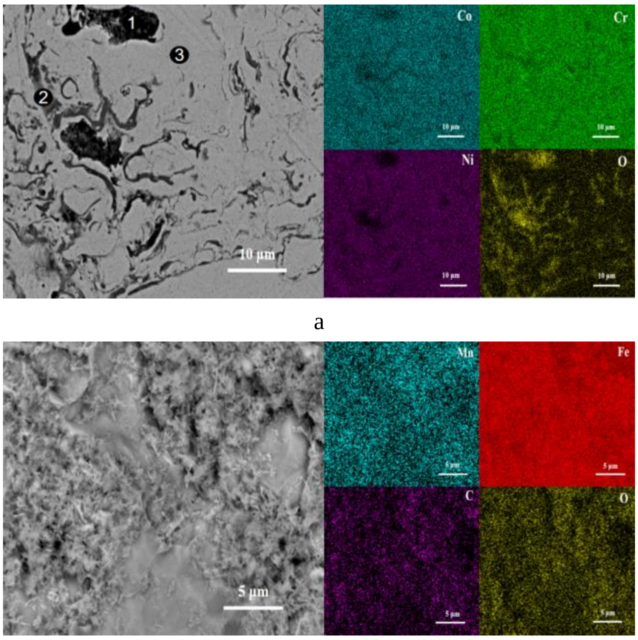

a

b

Fig. 11. SEM morphologies and EDS mapping: a – CoCrNi coating; b – 45 carbon steel after immersion in 3.5 wt.% NaCl solutions

Table 3. The corresponding EDS results indicated in Fig. 11 a

Position	Co, at.%	Cr, at.%	Ni, at.%	O, at.%
1	14.29	28.08	5.57	51.30
2	21.07	21.40	20.29	37.24
3	32.03	34.38	31.54	2.04

Fig. 12 shows the surface morphologies of the CoCrNi coatings and 45 carbon steel after immersion in 0.1 M NaOH solution at room temperature. A small number of corrosion pits and pronounced intergranular corrosion are observed on the corroded surface, with corrosion products predominantly localized at grain boundaries, as shown in Fig. 12 a. The main chemical components of the black and light grey zones in the CoCrNi coating are listed in Table 4. The results indicate minor selective dissolution of Cr and Ni elements, attributed to the active dissolution of Cr and Ni at grain boundaries and the attack of OH$^-$ on Cr/Ni$^-$depleted zones. The corrosion pits (approximately 1 – 2 µm in diameter) likely originate from the breakdown of the passive film at inherent coating defects, while the alkaline environment promotes the deposition of corrosion products in the form of hydroxides.

Table 2. The electrochemical parameters estimated from polarization data for the CoCrNi coating and 45 carbon steel in 3.5 wt.% NaCl solution and 0.1 M NaOH solution

Sample	*B*a,V per decade	*B*c, V per decade	E_{corr},V$_{SCE}$	I_{corr}, µA/cm^2	*R*, Ω
45 carbon steel (NaCl)	10.451	3.031	-0.677 ±0.02	50.9±0.04	633.3
CoCrNi coating (NaCl)	2.278	3.998	-0.217±0.01	0.26±0.08	260071.1
45 carbon steel (NaOH)	3.963	6.930	-0.519±0.03	1.43±0.05	28015.2
CoCrNi coating (NaOH)	5.797	6.102	-0.282±0.02	0.04±0.01	924605.0

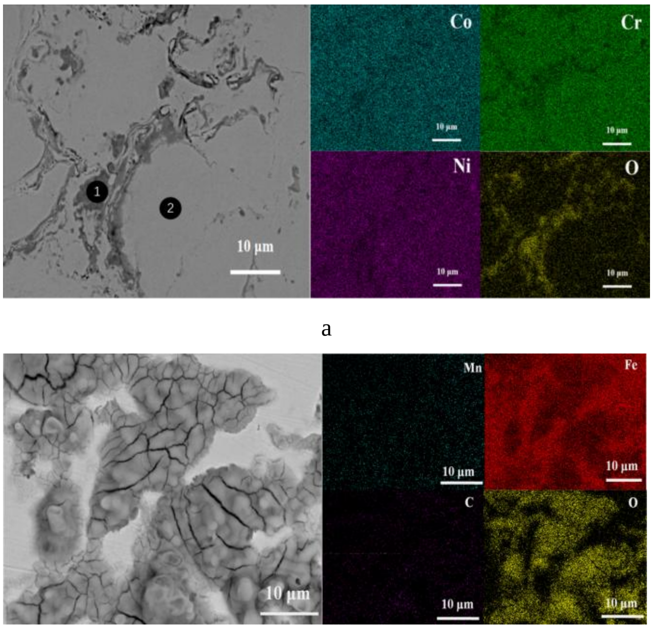

a

b

Fig. 12. SEM morphologies and EDS mapping of CoCrNi coating: a – CoCrNi coating; b – 45 carbon steel after immersion in 0.1M NaOH solutions

Table 4. The corresponding EDS results indicated in Fig. 12(a)

Position	Co, at.%	Cr, at.%	Ni, at.%	O, at.%
1	18.80	15.76	14.32	51.11
2	34.33	32.55	31.69	1.44

A large amount of dark colored corrosion products, which have been proven to be iron oxides, can be found on the surface of 45 carbon steel as shown in Fig. 12 b. Note here, a large number of microcracks formed on the surface of iron oxides. As a result, the oxide film has no significant passivation effect owing to OH^- diffusing through microcracks to contact the substrate, and leading to further corrosion. The electrochemical reaction of 45 carbon steel in NaOH solutions was oxygen absorption corrosion with a reaction equation of $4Fe+3O_2+H_2O \rightarrow Fe(OH)_3$. And $Fe(OH)_3$ can be further decomposed into iron oxide ($Fe_2O_3 \cdot xH_2O$), which is commonly known as rust.

4. CONCLUSION

CoCrNi MEA coating was prepared on the surface of 45 carbon steel by HVOF spraying. The wear resistance in a wide temperature range and corrosion resistance of CoCrNi coatings were investigated. The main conclusions are listed as follows:

The friction coefficient, depth and width of wear mark and average wear mass loss of the HVOF coatings are obviously reduced as friction temperature increased from RT to 200, 400 and 600 °C. CoCrNi coating has superior wear resistance during high temperature wear test.

Abrasive wear, fatigue wear, and plastic deformation were the main wear mechanisms during room temperature friction. With increasing of friction temperature, the oxidation degree of coatings intensified. And oxidative wear became the main wear mechanism under 600 °C. Abrasive wear, adhesive wear, and fatigue wear were auxiliary wear mechanisms.

E_{corr} and I_{corr} of CoCrNi coatings in NaCl solution were approximately (-0.217 ± 0.01) mV and (0.26 ± 0.08) $\mu A/cm^2$, respectively. Those of 45 steels were (-0.677 ± 0.02) mV and (50.9 ± 0.04) $\mu A/cm^2$, respectively. In addition, E_{corr} and I_{corr} of CoCrNi coatings in NaOH solution were approximately (-0.282 ± 0.02) mV and (0.04 ± 0.01) $\mu A/cm^2$, respectively. Those of 45 carbon steels were (-0.519 ± 0.03) mV and (1.43 ± 0.05) $\mu A/cm^2$, respectively. The corrosion resistances of CoCrNi coatings were more superior than those of 45 carbon steel both in NaCl and NaOH solutions.

Acknowledgments

The authors would like to thank Mr. M.H. Yang and Z. Xie, Mrs. S.Y. Yang and J.Y. Hu, Hunan MAG New Material Technology Co. Ltd, for their assistance in providing characterization services to this study. This work was supported by Natural Science Foundation of Hunan Province of China (Grant No. 2025JJ50287), Key Research and Development Program of Hunan Province of China (2022GK2030).

REFERENCES

1. **Tsai, M.H., Yeh, J.W.** High-entropy Alloys: A Critical Review *Materials Research Letters* 2 (3) 2014: pp. 107 – 123. https://doi.org/10.1080/21663831.2014.912690
2. **Yeh, J.W.** Physical Metallurgy of High-entropy Alloys *JOM* 67 (10) 2015: pp. 2254 – 2261. https://doi.org/10.1016/B978-0-12-816067-1.00003-5
3. **Yeh, J.W., Chen, S.K., Lin, S.J., Gan, J.Y., Chin, T.S., Shun, T.T., Chang, S.Y.** Nanostructured High-entropy Alloys with Multiple Principal Elements: Novel Alloy Design Concepts and Outcomes *Advanced Engineering Materials* 6 (5) 2004: pp. 299 – 303. https://doi.org/10.1002/adem.200300567
4. **Jo, Y.H., Jung, S., Choi, W.M., Sohn, S.S., Kim, H.S., Lee, B.J., Lee, S.** Cryogenic Strength Improvement by Utilizing Room-temperature Deformation Twinning in A Partially Recrystallized VCrMnFeCoNi High-entropy Alloy *Nature Communications* 8 2017: pp. 15719. https://doi.org/10.1038/ncomms15719
5. **Sathiyamoorthi, P., Basu, J., Kashyap, S., Pradeep, K.G., Kottada, R.S.** Thermal Stability and Grain Boundary Strengthening in Ultrafine-grained CoCrFeNi High-entropy Alloy Composite *Materials & Design* 134 2017: pp. 426 – 433. https://doi.org/10.1016/j.matdes.2017.08.053
6. **Zhang, A., Han, J., Su, B., Li, P., Meng, J.** Microstructure, Mechanical Properties and Tribological Performance of CoCrFeNi High-entropy Alloy Matrix Self-lubricating Composite *Materials & Design* 114 2017: pp. 253 – 263. https://doi.org/10.1016/j.matdes.2016.11.072
7. **Shang, C., Axinte, E., Sun, J., Li, X., Li, P., Du, J., Wang, Y.** CoCrFeNi ($W_{1-x}Mo_x$) High-entropy Alloy Coatings with Excellent Mechanical Properties and

Corrosion Resistance Prepared by Mechanical Alloying and Hot Pressing Sintering *Materials & Design* 117 2017: pp. 193 – 202. https://doi.org/10.1016/j.matdes.2016.12.076

8. **Praveen, S., Kim, H.S.** High-entropy Alloys: Potential Candidates for High-temperature Applications – An Overview *Advanced Engineering Materials* 20 (1) 2018: pp. 1700645. https://doi.org/10.1002/adem.201700645

9. **Sathiaraj, G.D., Skrotzki, W., Pukenas, A., Schaarschuch, R., Immanuel, R.J., Panigrahi, S.K., Kumar, S.S.** Effect of Annealing on The Microstructure and Texture of Cold Rolled CrCoNi Medium-entropy Alloy *Intermetallics* 101 2018: pp. 87 – 98. https://doi.org/10.1016/j.intermet.2018.07.014

10. **Yoshida, S., Bhattacharjee, T., Bai, Y., Tsuji, N.** Friction Stress and Hall-Petch Relationship in CoCrNi Equi-atomic Medium Entropy Alloy Processed by Severe Plastic Deformation and Subsequent Annealing *Scripta Materialia* 134 2017: pp. 33 – 36. https://doi.org/10.1016/j.scriptamat.2017.02.042

11. **Alhafez, I.A., Ruestes, C.J., Zhao, S., Minor, A.M., Urbassek, H.M.** Dislocation Structures Below a Nano-indent of The CoCrNi Medium-entropy Alloy *Materials Letters* 283 2021: pp. 128821. https://doi.org/10.1016/j.matlet.2020.128821

12. **Wetzel, A., von der Au, M., Dietrich, P.M., Radnik, J., Ozcan, O., Witt, J.** The Comparison of The Corrosion Behavior of The CrCoNi Medium Entropy Alloy and CrMnFeCoNi High Entropy Alloy *Applied Surface Science* 601 2022: pp. 154171. https://doi.org/10.1016/j.apsusc.2022.154171

13. **He, Q.F., Ye, Y.F., Yang, Y.** Formation of Random Solid Solution in Multicomponent Alloys: from Hume-Rothery Rules to Entropic Stabilization *Journal of Phase Equilibria and Diffusion* 38 2017: pp. 416 – 425. https://doi.org/10.1007/s11669-017-0560-9

14. **Gludovatz, B., Hohenwarter, A., Thurston, K.V., Bei, H., Wu, Z., George, E.P., Ritchie, R.O.** Exceptional Damage-tolerance of A Medium-entropy Alloy CrCoNi at Cryogenic Temperatures *Nature Communications* 7 2016: pp. 10602. https://doi.org/10.1038/ncomms10602

15. **Rodriguez, A., Tylczak, J. H., Ziomek-Moroz, M.** Corrosion Behavior of CoCrFeMnNi High-entropy Alloys (HEAs) under Aqueous Acidic Conditions *ECS Transactions* 77 2017: pp. 741. https://doi.org/10.1149/07711.0741ecst

16. **Luo, H., Li, Z., Mingers, A.M., Raabe, D.** Corrosion Behaviorof an Equiatomic CoCrFeMnNi High-entropy Alloy Compared with 304 Stainless Steel in Sulfuric Acid Solution *Corrosion Science* 134 2018: pp. 131 – 139. https://doi.org/10.1016/j.corsci.2018.02.031

17. **Cao, F., Munroe, P., Zhou, Z., Xie, Z.** Medium Entropy Alloy CoCrNi Coatings: Enhancing Hardness and Damage-tolerance Through A Nanotwinned Structuring *Surface and Coatings Technology* 335 2018: pp. 257 – 264. https://doi.org/10.1016/j.surfcoat.2017.12.021

18. **Li, C.L., Hsueh, C.H.** Effects of Cerium Addition on Microstructures and Mechanical Properties of CoCrNi Medium Entropy Alloy Films *Surface and Coatings Technology* 424 2021: pp. 127645. https://doi.org/10.1016/j.surfcoat.2021.127645

19. **Chen, Y., Zhou, Z., Munroe, P., Xie, Z.** Hierarchical Nanostructure of CrCoNi Film Underlying Its Remarkable Mechanical Strength *Applied Physics Letters* 113 2018: pp. 5042148. https://doi.org/10.1063/1.5042148

20. **Feng, K., Zhang, Y., Li, Z., Yao, C., Yao, L., Fan, C.** Corrosion Properties of Laser Cladded CrCoNi Medium Entropy Alloy Coating *Surface and Coatings Technology* 397 2020: pp. 126004. https://doi.org/10.1016/j.surfcoat.2020.126004

21. **Xue, P., Zhu, L., Xu, P., Ren, Y., Xin, B., Meng, G., Liu, Z.** Research on Process Optimization and Microstructure of CrCoNi Medium-entropy Alloy Formed by Laser Metal Deposition *Optics & Laser Technology* 142 2021: pp. 107167. https://doi.org/10.1016/j.optlastec.2021.107167

22. **Zhang, Z., Zhang, B., Zhu, S., Tao, X., Tian, H., Wang, Z.** Achieving Enhanced Wear Resistance in CoCrNi Medium-entropy Alloy Co-Alloyed with Multi-Elements *Materials Letters* 313 2022: pp. 131650. https://doi.org/10.1016/j.matlet.2022.131650

23. **Koga, G.Y., Nascimento, A.R.C., Ettouil, F.B., Rodrigues, L.C.M., Zepon, G., Bolfarini, C., Coury, F.G.** Thermally Sprayed Multi-principal Element $Cr_{40}Co_{40}Ni_{20}$ Coatings-Oxidation upon Coatings' build-up and Electrochemical Corrosion *Surface and Coatings Technology* 454 2023: pp. 129154. https://doi.org/10.1016/j.surfcoat.2022.129154

24. **Yu, H., Xu, Z., Zhang, X., He, Y., Jia, X.** Corrosion Behaviour of HVOF-sprayed CoCrNi Coating on Copper Alloy Surface in NaCl Solution *JOM* 76 2024: pp. 3161 – 3171. https://doi.org/10.1007/s11837-024-06562-x

25. **Huang, D., Xu, Z., Jia, X., Yu, H., He, Y., Dong, Z., Zhang, H.** Uniform Microstructure and Excellent Corrosion Resistance of HVOF-Sprayed CoCrNi Medium-entropy Alloy Coating in Fluoride Ion Environment *Metals and Materials International* 30 2024: pp. 61 – 76. https://doi.org/10.1007/s12540-023-01475-x

26. **Wang, Y., Zhang, W., Chen, D., Liu, X., Hu, W., Liu, L., Xiong, X.** High Temperature Friction and Wear Performance of TiB_2-50Ni Composite Coating Sprayed by HVOF Technique *Surface and Coatings Technology* 407 2021: pp. 126766. https://doi.org/10.1016/j.surfcoat.2020.126766

27. **Liu, S., Peng, Y., Zhang, Y., Wang, Y., Fan, W., Wang, A., Lan, Y.** Effect of Nanostructure on Wear and Corrosion Behavior of HVAF-sprayed Eutectic High-entropy Alloy Coatings *Journal of Thermal Spray Technology* 31 2022: pp. 1252 – 1262. https://doi.org/10.1007/s11666-022-01342-y

28. **Xie, L., Xiong, X., Zeng, Y., Wang, Y.** The Wear Properties and Mechanism of Detonation Sprayed Iron-based Amorphous Coating *Surface and Coatings Technology* 366 2019: pp. 146 – 155. https://doi.org/10.1016/j.surfcoat.2019.03.028

29. **Xie, L., Wang, Y.M., Xiong, X., Chen, Z.K.** Comparison of Microstructure and Tribological Properties of Plasma, High Velocity Oxy-fuel and Detonation Sprayed Coatings from An Iron-based Powder *Materials Transactions* 59 2018: pp. 1591 – 1595. https://doi.org/10.2320/matertrans.M2018141

30. **Wang, Y.M., Xie, L., Wu, X.L., Li, C.L., Zhou, P.** Microstructure and Tribological Properties of FeCoCrNi

High-entropy Alloy Coatings Fabricated by Atmospheric Plasma Spraying *Journal of Materials Engineering and Performance* 32 2023: pp. 3475 – 3486. https://doi.org/10.1007/s11665-022-07331-0

31. **Wang, J., Li, W., Yang, H., Huang, H., Ji, S., Ruan, J., Liu, Z.** Corrosion Behavior of CoCrNi Medium-entropy Alloy Compared with 304 Stainless Steel in H_2SO_4 and NaOH Solutions *Corrosion Science* 177 2020: pp. 108973. https://doi.org/10.1016/j.corsci.2020.108973

32. **Chang, S.H., Liang, C.H., Huang, K.T., Liang, C.** Evaluation of The Microstructures, Strengthening Mechanisms and Corrosion Behaviors of TiB_2 Powder Added to Ti-8Ta-6Ni Alloys Through The Vacuum Sintering Process *Journal of Alloys and Compounds* 857 2021: pp. 157629. https://doi.org/10.1016/j.jallcom.2020.157629

33. **Wang, Z.H., Ma, X.R., Gao, Y.** Study on Corrosion Behavior of 45 Steel in NaCl Solution *Journal of Gansu Sciences* 33 (2) 2021: pp. 67 – 70. https://doi.org/10.16468/j.cnki.issn1004-0366.2021.02.012